

Effects of geometry and intermetallic bonding on the mechanical response, spalling and fragmentation of Ni–Al laminates

Efrem Vitali^a, Chung-Ting Wei^b, David J. Benson^{c,*}, Marc A. Meyers^b

^a Lawrence Livermore National Laboratory, CA, USA

^b Department of Mechanical and Aerospace Engineering, University of California, San Diego, CA, USA

^c Department of Structural Engineering, University of California, San Diego, CA, USA

Received 28 April 2011; received in revised form 20 May 2011; accepted 23 May 2011

Available online 4 July 2011

Abstract

Conventional uniaxial tension tests and laser-shock experiments were carried out to investigate the mechanical properties of aluminum–nickel laminates under quasi-static ($\sim 10^{-3} \text{ s}^{-1}$) and dynamic ($\sim 10^5 \text{ s}^{-1}$) loading conditions. A finite-element code was used to model the experiments and provide insights into the laminates' mechanical response. It was demonstrated that the geometry of the laminate constituents (i.e. the aluminum and nickel laminae) and the interlaminar bonding are the two critical parameters in determining the accuracy of the numerical calculations. These results are also useful to those interested in improving the mechanical properties of this class of materials since we demonstrate that a material with “perfect” laminae and “perfect bonding” is substantially stronger than the experimental material.

© 2011 Acta Materialia Inc. Published by Elsevier Ltd. All rights reserved.

Keywords: Simulation; Laser; Shocks; Layered structures; Interface structures

1. Introduction

Many commercial materials have a laminar microstructure, ranging from the sub-microscale in integrated circuits to the macroscale of the nickel–copper laminate used in the US quarter-dollar coin. The search for composite structures with specific mechanical properties requires scientists to analyze the behavior of different combinations of materials tested under different loading conditions. Investigating the mechanical behavior of materials is challenging at high strain rates. Many of the standard experimental methods yield only the final state of the material without any time-resolved data. Numerical simulations are often used to gain insight into the dynamic process. Their effectiveness, however, depends on the accuracy of the numerical model. The appropriateness of the model for a specific experiment can be evaluated by a careful characterization

of the ab initio state of the experiment followed by a comparison of the numerical results against the post-mortem state of the experiment.

The current research focuses on Ni–Al laminates. The motivation for the choice of the Ni–Al is threefold. First, this is a reactive mixture amenable to combustion synthesis, an important technological process for the production of intermetallics, composites and ceramics [1]. Second, this system is currently being used as a heat source and for joining components. Third, there is significant interest in developing shell casings that react exothermically under shock wave loading caused by detonation, augmenting the kinetic energy with the exothermic chemical energy.

In recent work, Wei et al. [1,2] carried out a series of experiments at the Lawrence Livermore National Laboratory to investigate the response of Ni–Al composites to laser-induced shocks. Our paper presents the experimental technique, post-impact characterization of the recovered material, and the computational modeling with the respective findings relevant to the accuracy of the model.

* Corresponding author. Tel.: +1 858 534 5928.

E-mail address: dbenson@ucsd.edu (D.J. Benson).

The experimental methods and results are discussed in Section 2, which describes the experiment and provides the basic parameters for the numerical model. The simulation methodology is presented in Section 3. The effects of the geometry on the numerical results are discussed in Section 4, while the role of the interlaminar bonding is explored in Section 5. The last section summarizes the results.

2. Quasi-static and dynamic experiments

The Ni–Al laminates, with two different bilayer thicknesses, 5 and 30 μm , were produced by cold rolling [3]. The laminates, with a total thickness of about 0.9 mm, were cut into 5×5 mm squares and subjected to strong shocks generated by the Janus Nd-glass laser at the Jupiter laser facility of Lawrence Livermore National Laboratory. Two series of laser shots, delivering 100 and 400 J, were conducted, at a wavelength of 532 nm and a pulse duration of 3 ns. The lasers irradiated the laminates directly with an injection angle at 27° to the laminate stacking direction. A face plate was used to smooth out the laser pulse irregularities. These laser energies can generate massive damage on the irradiated surface [4,5], induce spall fracture and produce fragments from the spalling surface [4–7].

Uniaxial tensile tests were conducted on laminates using an Instron Universal Test Machine 3370. Two different test orientations were chosen for studying the anisotropic mechanical properties of the laminates in the transverse and longitudinal directions. The transverse tension tests had the tensile direction parallel to the stacking axis. The laminates were machined to 2×2 mm squares and glued with fixtures as shown in Fig. 1a. The longitudinal tension tests had the tensile direction perpendicular to the stacking axis. The samples were machined to a dog-bone shape by electric discharge machining with the neck of the dog-bone being 2 mm long and 1 mm wide, as shown in Fig. 1b.

Fig. 2 shows the cross-sections of two different laminates characterized by field emission scanning electron microscopy (SEM, Philips). The thicker bilayer sample had regions of localized shear deformation, which results in

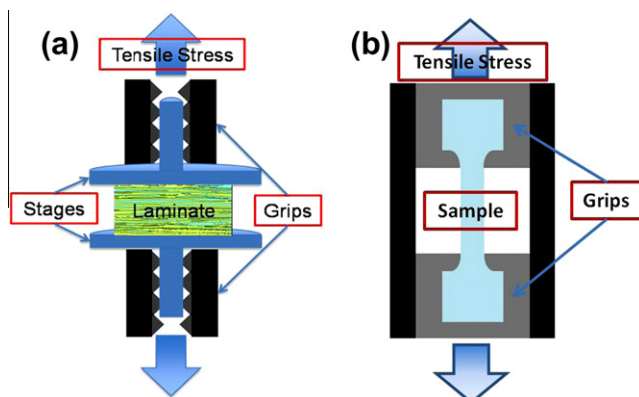


Fig. 1. Schematics of the tensile tests: (a) transverse direction and (b) longitudinal direction.

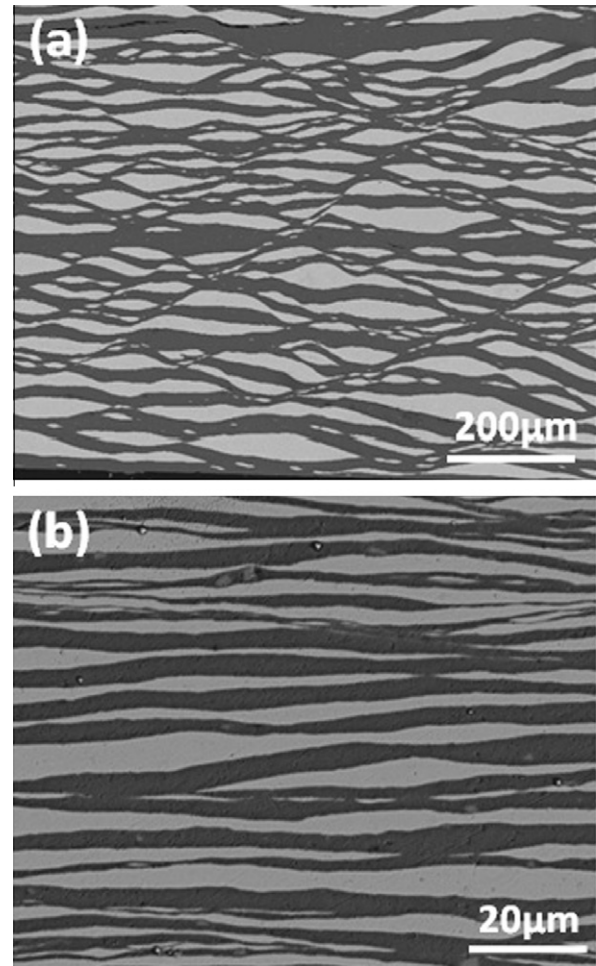


Fig. 2. Cross-sections of (a) thick bilayer (30 μm) and (b) thin bilayer (5 μm) laminates.

the wave-like cross-sectional morphology shown in Fig. 2a, while the thinner bilayer sample had a more regular laminar structure shown in Fig. 2b. It should be noted that in the back-scattered image of SEM, the brighter area represents the lighter material, aluminum, and the darker area represents the heavier material, nickel.

2.1. Quasi-static test results

The longitudinal and transverse tensile test results, shown in Fig. 3a and b, show the anisotropic mechanical properties of the cold-rolled laminates. In the longitudinal tensile direction, the stress–strain curves show that the laminates have almost no plastic deformation. The laminar structure strains elastically and fractures after a certain amount of elastic deformation. Although the elastic curves allow the Young's modulus to be measured (varying from ~ 15 to ~ 80 GPa), these values cannot be applied reliably, since no strain gage extensometer was used. Hence, the curves are only used to extract the maximum stress.

The transverse tensile tests show that the thick bilayer laminates have higher failure strengths than the thin bilayer

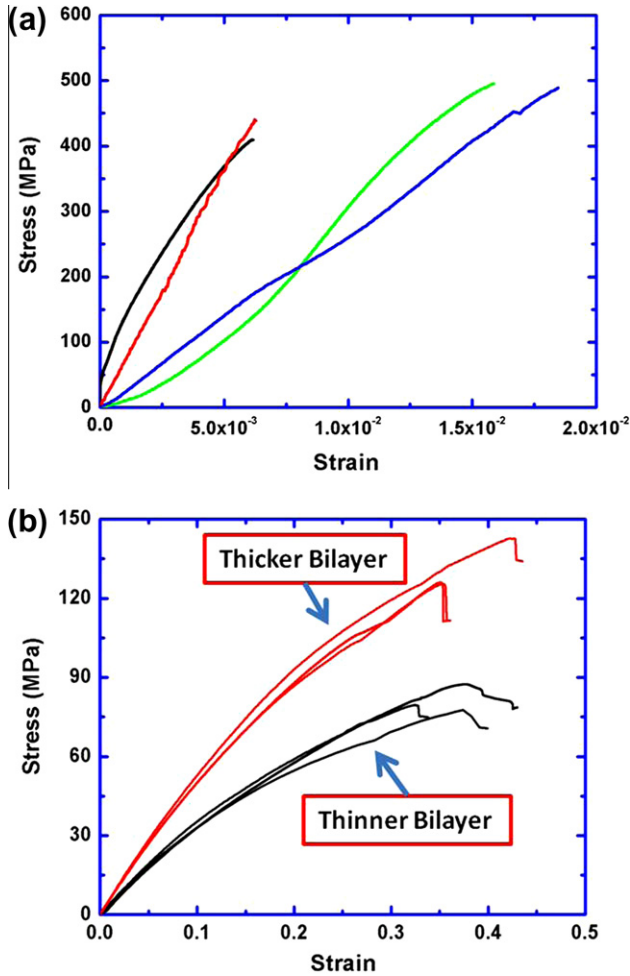


Fig. 3. Tensile tests: (a) longitudinal direction tests and (b) transverse direction tests.

laminates, suggesting that the thick bilayer samples might have fewer defects, or pre-existing cracks, caused by the cold-rolling process. The tensile curves show an apparent plastic response that is caused by the gradual delamination.

2.2. Weibull statistical analysis

Weibull analysis is commonly used to characterize the stochastic response of engineering materials. The plastic deformation of a ductile material is usually sufficient to compensate for the effects of flaws on its strength. However, for brittle materials, pre-existing defects are responsible for catastrophic failure. Owing to the variations in orientation, size and distribution of defects, the failure strength of brittle materials can vary significantly from specimen to specimen [8,9]. The typical Weibull analysis utilizes the relation between the failure probability, F , and the failure strength, σ , to evaluate the suitability of the material for engineering applications:

$$F = 1 - P = 1 - \exp \left[- \left(\frac{\sigma - \sigma_u}{\sigma_o} \right)^m \right] \quad (1)$$

where P is the survival probability, σ_u is the smallest failure strength, σ_o is the characteristic strength, and the m is the Weibull modulus. A large Weibull modulus indicates that the the sample-to-sample variation of failure strength is small, allowing smaller safety factors in engineering design. The Weibull distribution can be rewritten as:

$$\ln \ln [1 - F] = -m(\ln(\sigma) - \ln(\sigma_o)) \quad (2)$$

where the σ_u is chosen to be zero. A plot of $\ln \ln [1/(1 - F)]$ vs. $\ln(\sigma/\sigma_o)$ for the laminates is shown in Fig. 4. The Weibull modulus is 3.4 for the longitudinal direction (\square) and 8.8 (\circ and \triangle) for the transverse direction. For comparison, the Weibull moduli of conventionally processed alumina, controlled particle size alumina and steel are 4.7, 9.7 and ∞ , respectively [8]. The longitudinal direction apparently has greater sample-to-sample variation compared to the transverse direction. This suggests that the rolling process can induce anisotropic fracture in the direction perpendicular to the longitudinal tensile orientation, producing a large variation in the longitudinal failure strengths.

The average failure strength for a material in a plot of $\ln \ln [1/(1 - F)]$ vs. $\ln(\sigma)$ occurs at the point where $\ln \ln [1/(1 - F)] = 0$. Here the σ_o is chosen as the arithmetic mean of the fracture stresses, measured from longitudinal and transverse tensile tests, which is about 381 and 102 MPa. From the fits of the longitudinal (\square) and transverse (\circ) data, the estimated average failure strengths are 450 and 114.5 MPa, respectively. The lower average failure strength of the material in the transverse direction significantly restricts the utility of the laminates.

2.3. Spalling and fragmentation of laser-shocked recovery samples

Spalling was investigated and the observed fragment sizes were correlated to calculated values based on the Grady–Kipp theory [6,7,10]. This theory is based on the energetic balance between, on one side, the kinetic energy of

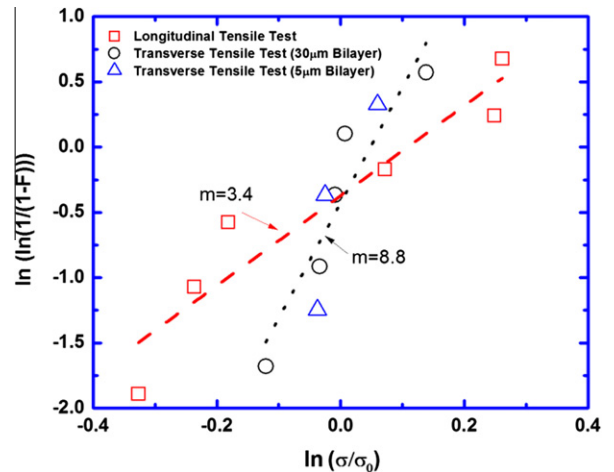


Fig. 4. Longitudinal and transverse tensile bonding test, where F is the probability of failure.

an expanding body, T , and the elastic energy U , and on the other side, the fracture energy W :

$$T + U > W. \quad (3)$$

This leads to predicted fragment sizes s for brittle failure:

$$s = 2 \left(\frac{\sqrt{3}K_c}{\rho C_0 \dot{\epsilon}} \right)^{2/3}, \quad (4)$$

and ductile failure:

$$s = \left(\frac{8\sigma_y \epsilon_c}{\rho \dot{\epsilon}^2} \right)^{1/2} \quad (5)$$

where K_c is the fracture toughness, ρ is the density, C_0 is the bulk sound velocity, $\dot{\epsilon}$ is the strain rate, σ_y is the yield strength, and ϵ_c is the critical strain. It should be noted that the fragmentation may change from brittle to ductile at high strain rates in the range of 10^6 – 10^7 s⁻¹.

Due to the strain-rate and temperature dependencies, Kipp et al. later modified the equations for spall [7]. For fracture toughness dominated spallation, they proposed:

$$s = \left(\frac{\sqrt{24}K_c}{\rho C_0 \dot{\epsilon}} \right)^{2/3} \quad (6)$$

and for flow stress dominated spallation:

$$s = \left(\frac{1.2\sigma_y}{\rho \dot{\epsilon}^2} \right)^{1/2}. \quad (7)$$

The differences between Eqs. (4) and (6), and Eqs. (5) and (7), are minor. The yield strength, σ_y , is given by:

$$\sigma_y = \sigma_y^0 \left(\frac{\dot{\epsilon}}{\dot{\epsilon}_0} \right)^m, \quad (8)$$

where the σ_y^0 is the reference yield strength, which is about 449.9 MPa from Section 2.2; the reference strain rate, $\dot{\epsilon}_0$, is

1s⁻¹; and m is the strain-rate sensitivity which was set as 0.1 (for steel) [7].

The two equations, for ductility and fracture toughness dominated fragmentation, were applied. It is possible to estimate the strain rate experienced by the spalled region as it bulges out of the back. This estimate can be obtained from the free surface velocity (U_{fs}) divided by the original size of the spall area (d) [4]. Fig. 5 shows the schematic of the crater formation and spalling on the back surface with the free surface velocity (U_{fs}) and spall diameter d .

The one-dimensional, Lagrangian hydrocode HYADES code [11] was used to estimate the pressures as the shock wave arrived at the free surface for the 100 and 400 J shots. HYADES is designed for simulations at high temperature where materials are ionized and radiation transport may be important. Fig. 6 shows the shock wave propagation for a 400 J laser energy shot at 13.4 ns after the laser irradiation. The stress fluctuates due to the interactions of the wave with the Ni and Al lamellae. The shock wave pressure attenuates to about 14 GPa at the depth of ~ 950 μ m. For the the 100 J laser, it was also estimated in the same way and is about 3.5 GPa.

The shock and particle velocities are estimated from the HYADES-predicted pressure by using the Hugoniot relationships and equation of state (EOS). A rule of mixtures was used to estimate a single value for the laminate, giving: C_0 (4950 m/s), S (1.4) and ρ_0 (5.83×10^3 kg/m³).

$$P = \frac{\rho_0}{S} (U_s^2 - C_0 U_s) \quad (9)$$

$$U_s = C_0 + S U_p \quad (10)$$

The free surface velocity is equal to $2U_p$. The spall diameter (d) was measured by two different approaches: by using the image-processing software ImageJ from direct inspection of SEM images; and by calculating an average diameter from the area measurement of the spall surface. The results

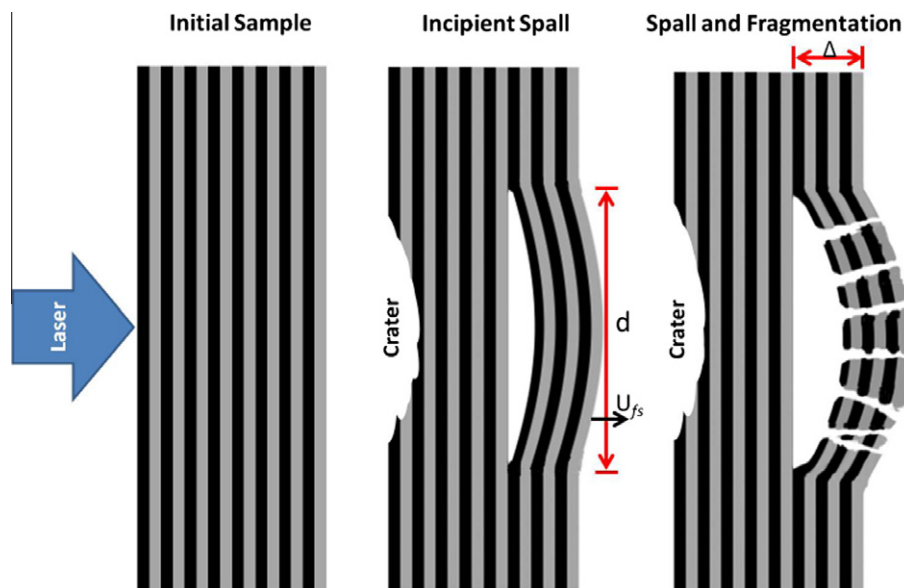


Fig. 5. Spallation and fragmentation sequence.

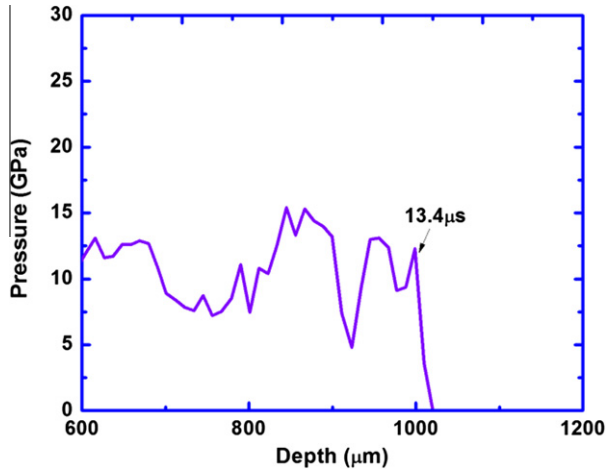


Fig. 6. HYADES simulation: 400 J, 3 ns, laser shock wave propagates to the rear surface of the laminate with bilayer thickness 30 μm.

of the free surface velocity and spall size, along with the calculated strain rates, are listed in Table 1. They are of the order of $1 - 5 \times 10^5 \text{ s}^{-1}$.

The yield strength, σ_y , obtained from Eq. (8) is about 1.6 GPa. From Eqs. (6) and (7), the calculated fragment sizes are about $2.7 \times 10^{-3} \text{ m}$ for ductile fracture and $9.3 \times 10^{-4} \text{ m}$ for brittle fracture, assuming K_c is equal to $40 \text{ MPa m}^{1/2}$ [7]. Detailed results are provided in Table 1. We also measured the sizes of the fragments collected in the recovery capsule. The average diameters of the fragments are shown in Table 1. In comparison with the calculated results, the measured fragment size was closer to the brittle fragment size estimation. There are significant differences: the Grady–Kipp fragment sizes are higher than the measured values by a factor of 5–10. There seems to be a scaling factor with bilayer thickness that is not incorporated into the simple Grady–Kipp model. It is possible that the thinner bilayer has more initiation sites for fracture. There are more refined treatments that predict smaller frag-

Table 1
Experimentally measured parameters and predictions from modified Grady–Kipp (G–K) equations (Kipp et al. [7], Eqs. (6) and (7)).

Laser energy	100 J	400 J
$U_{fs} = 2U_p$	234.8 m s^{-1}	864.6 m s^{-1}
Spall size for 5 μm bilayer sample	$1.51 \pm 0.5 \text{ (mm)}$	$1.59 \pm 0.35 \text{ (mm)}$
Spall size for 30 μm bilayer sample	$1.85 \pm 0.79 \text{ (mm)}$	$1.94 \pm 0.78 \text{ (mm)}$
Strain rate (for 5 μm)	$1.6 \times 10^5 \text{ s}^{-1}$	$5.4 \times 10^5 \text{ s}^{-1}$
Strain rate (for 30 μm)	$1.2 \times 10^5 \text{ s}^{-1}$	$4.5 \times 10^5 \text{ s}^{-1}$
G–K ductile fragment size (for 5 μm)	3.68 mm	1.09 mm
G–K ductile fragment size (for 30 μm)	4.91 mm	1.31 mm
G–K brittle fragment size (for 5 μm)	1.22 mm	0.54 mm
G–K brittle fragment size (for 30 μm)	1.47 mm	0.61 mm
Measured fragment size (for 5 μm)	0.43 mm	0.13 mm
Measured fragment size (for 30 μm)	0.46 mm	0.43 mm

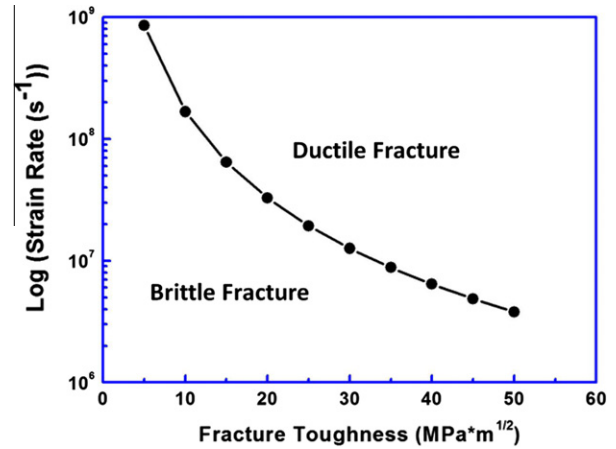


Fig. 7. Critical strain rate vs. fracture toughness.

ments, such as the ones by Glenn and Chudnovsky [12] and Zhou et al. [13]. They predict sizes that are smaller than the Grady–Kipp by a factor of 6.

Kipp et al. [7] proposed that the critical strain rate for brittle–ductile transition can be obtained by setting Eq. (4) equal to Eq. (5) (or alternatively, setting Eqs. (6) and (7) equal). The result is:

$$\dot{\epsilon}_t = \left(k C_0^2 \rho^{1/2} \sigma_y^{2/3} \epsilon^{2/3} \right) K_c^{-2} \quad (11)$$

where K_c and σ_y are the reference fracture toughness and yield strength and k is a parameter (equal to 0.94 for Eqs. (4) and (5)). Incorporating the strain-rate-dependent yield stress, Eq. (7), into Eq. (11), the brittle–ductile transition point is approximately $5 \times 10^6 \text{ s}^{-1}$ for this experiment. Fig. 7 shows the change in the critical strain rate as a function of K_c . Since the strain rate from our estimation was lower than 10^6 s^{-1} , the fracture toughness dominated spallation model was used to estimate the fracture toughness of the laminar samples.

3. The simulation methodology

The mechanical response of the laminate was simulated with Raven [14–20], a two-dimensional Eulerian finite-element research code developed at UCSD. The pressure profile generated from the interaction between the laser beam and the material is obtained from HYADES [11], a one-dimensional radiation hydrodynamics code.

Although the system is conceptually simple (alternating layers of Ni and Al subjected to a shock generated by a laser), obtaining simulation results that matched reasonably well with the experiments proved to be a challenge. A wide range of parameter studies was performed. In the end, the model was found to require an accurate description of the layer morphology and an accurate model of the Ni–Al interface debonding to generate an accurate agreement with the experiments. The modeling of the layer morphology and the debonding are therefore the primary topics in this section. A brief description of the material model and EOS are provided for completeness.

3.1. Material model and equation of state

The Johnson–Cook plasticity model [21] and the Grüneisen EOS were used to model the metals. The results were not very sensitive to the values of the Johnson–Cook material parameters and many other models would have worked as well.

The yield stress for the Johnson–Cook model is:

$$\sigma_y = [A + B(\bar{\epsilon}^p)^n][1 + C \ln(\dot{\epsilon}^{\star})][1 - T^{\star m}], \quad (12)$$

and the normalized strain rate $\dot{\epsilon}^{\star}$ and temperature T^{\star} are:

$$\dot{\epsilon}^{\star} = \frac{\dot{\epsilon}}{\dot{\epsilon}_o} \quad \text{for} \quad \dot{\epsilon}_o = 1.0 \frac{1}{s} \quad (13)$$

$$T^{\star} = \frac{T - T_{ROOM}}{\Delta T} \quad \text{where} \quad \Delta T = T_{MELT} - T_{ROOM} \quad (14)$$

where A , B , n , C and m are material parameters, $\bar{\epsilon}^p$ is the equivalent plastic strain, $\dot{\epsilon}$ is the strain rate, T is the temperature, e is the specific internal energy, C_p is the specific heat, and σ_y is the yield stress. The first term enclosed in square brackets on the right-hand side of Eq. (12) includes the nominal yield stress (i.e. A) and defines the strain hardening; the second and third terms in the square brackets describe the strain rate and temperature dependencies, respectively. The damage $\mathcal{D} \in [0, 1]$ is defined as:

$$\mathcal{D} = \int_0^{\epsilon^f} \frac{\dot{\epsilon}^p(\tau)}{\epsilon^f} d\tau \quad (15)$$

and the failure strain, ϵ^f , is:

$$\epsilon^f = [D_1 + D_2 \exp(D_3 \sigma^{\star})][1 + D_4 \ln(\dot{\epsilon}^{\star})][1 + D_5 T^{\star}] \quad (16)$$

$$\sigma^{\star} = - \frac{P}{\sqrt{\frac{3}{2} \sigma' : \sigma'}} \quad (17)$$

where D_1 – D_5 are the damage parameters, $\dot{\epsilon}^p$ is the effective plastic strain rate, P is the pressure, and σ' is the deviatoric part of the stress tensor. Table 2 shows the constants used in the material model for Al and Ni.

The Grüneisen EOS is:

$$P = \frac{\rho_0 C_0^2 \mu \left[1 + \left(1 - \frac{\Gamma_0}{2} \right) \mu - \frac{a_0 \mu^2}{2} \right]}{\left[1 - (S_1 - 1) \mu - \frac{S_2 \mu^2}{(\mu+1)} - \frac{S_3 \mu^3}{(\mu+1)^2} \right]^2} + (\Gamma_0 + a_0 \mu) E \quad \text{for} \quad \mu \geq 0 \quad (18)$$

$$P = \rho_0 C_0^2 \mu + (\Gamma_0 + a_0 \mu) E \quad \text{for} \quad \mu < 0 \quad (19)$$

$$\mu = \frac{P}{\rho_0} - 1 \quad (20)$$

Table 2
Material parameters.

	ρ_0 (g cm ⁻³)	G (g μs ⁻² cm ⁻¹)	A (g μs ⁻² cm ⁻¹)	B (g μs ⁻² cm ⁻¹)	n	C	m
Al	2.768	0.262	4.3×10^{-3}	4.26×10^{-3}	0.34	1.5×10^{-2}	1.0
Ni	8.902	0.7446	7.66×10^{-3}	6.481×10^{-3}	0.33	6.0×10^{-3}	1.44
	C_p (cm ² μs ⁻² K ⁻¹)	ΔT (K)	D_1	D_2	D_3	D_4	D_5
Al	8.75×10^{-6}	480.6	0.13	0.13	-1.5	1.1×10^{-2}	0.0
Ni	4.463×10^{-6}	1432.0	0.0	4.04	-1.84	0.0	0.0

where C_0 , S_1 , S_2 , S_3 , Γ_0 and a_0 are material properties, ρ_0 is the initial density, ρ is the current density, and E is the energy per reference volume. Table 3 provides the constants used in the EOS for the two materials [22].

3.2. Geometry and boundary conditions

Fig. 8 shows the initial geometry of the problem where layers of uniform thickness were used to model the composite. Only one-half of the domain was modeled due to symmetry. Materials 1 and 2 represent the Ni and Al laminae, respectively, which form the 864 μm thick laminate, while material 3 symbolizes the laser beam. The problem domain is 1 mm wide and 2 mm thick, and employs a mesh of 240×384 elements. The mesh size was chosen such that each lamina has a minimum of approximately four elements in the vertical direction to adequately resolve bending phenomena in the layers. Convergence studies demonstrated that this was adequate. The left boundary is constrained in the normal direction, while the right boundary is fixed in both directions, and the bottom and top boundaries are free. The right, top and left boundaries of the material modeling the laser beam are constrained in the normal direction. The constraints on the beam boundaries are released once its pressure has dropped to zero.

3.3. Modeling the laser loading

The pressure generated by the laser beam was calculated with the one-dimensional HYADES hydrocode [11], then applied as a time-dependent pressure boundary condition to the upper surface of the composite in the two-dimensional simulation with Raven. To simplify the application of the boundary condition, which is applied to the interior of the computational mesh, a phony gas material (material 3 in Fig. 8), having the appropriate pressure–time history, was numerically confined to the appropriate region adjacent to the upper layer of the laminate. Fig. 9 displays a schematic representation of the one-dimensional HYADES

Table 3
Parameters for the equation of state.

	C_0 (cm μs ⁻¹)	S_1 (-)	S_2 (-)	S_3 (-)	Γ_0 (-)	a_0 (-)
Aluminum	0.5328	1.338	0.0	0.0	2.0	0.48
Nickel	0.465	1.445	0.0	0.0	1.93	0.5

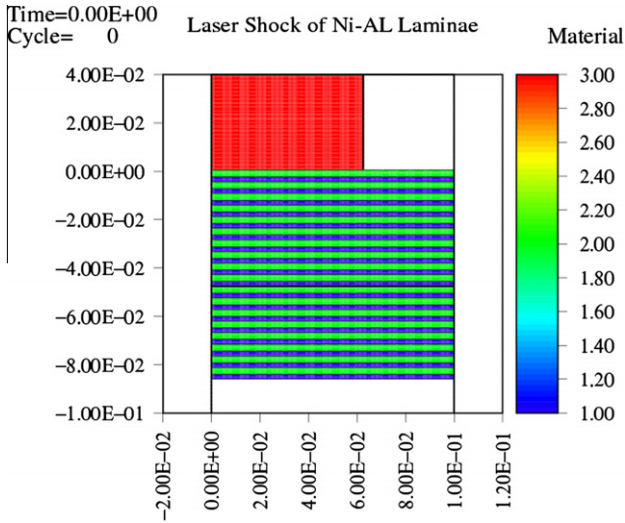


Fig. 8. Idealized geometry: initial conditions.



Fig. 9. HYADES model representation.

model, which consists of a 1.0 cm long Al body and a 105 J laser beam.

A 200 element mesh defines the first 0.05 cm of the body, where the size of the elements increases constantly by a factor of 1.04 to avoid a numerical shock impedance mismatch between adjacent elements, and only one element is used to represent the remaining portion of the body. The laser beam strikes the aluminum with a 3 ns square pulse from the side with the smallest element (i.e. left side in Fig. 9).

Fig. 10 shows the pressure–time history obtained from HYADES along with the smoothed loading curve used in the Raven input file. The fluctuations in the pulse are due to the stress interactions along the interfaces and the difference of the impedance between Ni and Al.

4. Sensitivity to composite geometry

The geometry of the real laminates in Fig. 2 is far from uniform. The role of the non-uniformity is evaluated by comparing the response of an idealized composite to one from a micrograph.

4.1. Composite lamina of uniform thickness

Fig. 11 displays the damage in the upper region of the laminate at 0.05 μ s (i.e. at the end of the loading cycle, see Fig. 10). As the shock wave moves through the first few layers of the laminate, the Al is instantaneously dam-

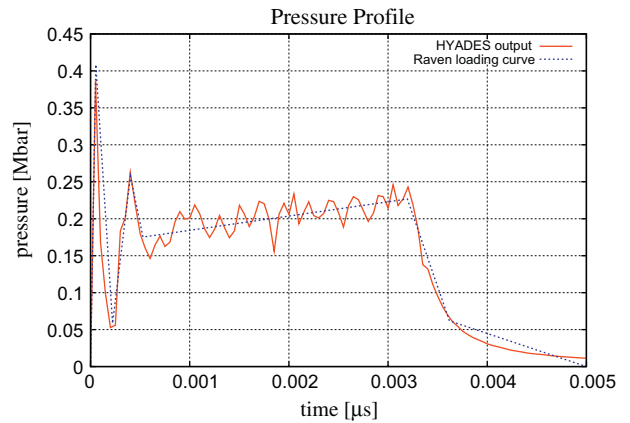


Fig. 10. Pressure–time history of the laser-generated shock in aluminum calculated with Hyades.

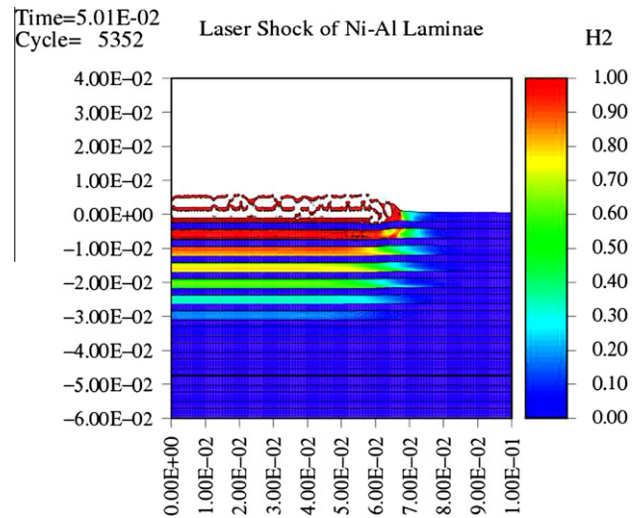


Fig. 11. Damage calculated for a composite with uniform layers.

aged whereas the damage in the Ni is contained. It is worth noting that the temperature generated in these layers is well below the melting point of the two materials.

Fig. 12 shows different stages of the simulation: the left, middle and right pictures display the vertical velocity at 1, 5 and 25 μ s, respectively. The first Al layer has disintegrated, while the second and third laminae (i.e. Ni and Al, respectively) spalled. The spall surface is located within the failed Al lamina because the failure of the interface bonding is not modeled in this series of calculations. While the behavior of the top layers is in rough qualitative agreement with the experimental results presented in Fig. 14b, the delamination in the middle of the specimen and the spall of the bottom layers are not predicted by this model.

4.2. Composite lamina imported via micrography

An accurate representation of the actual geometry of the composite lamina is necessary to improve the quality of the solution. There are a number of approaches that could be

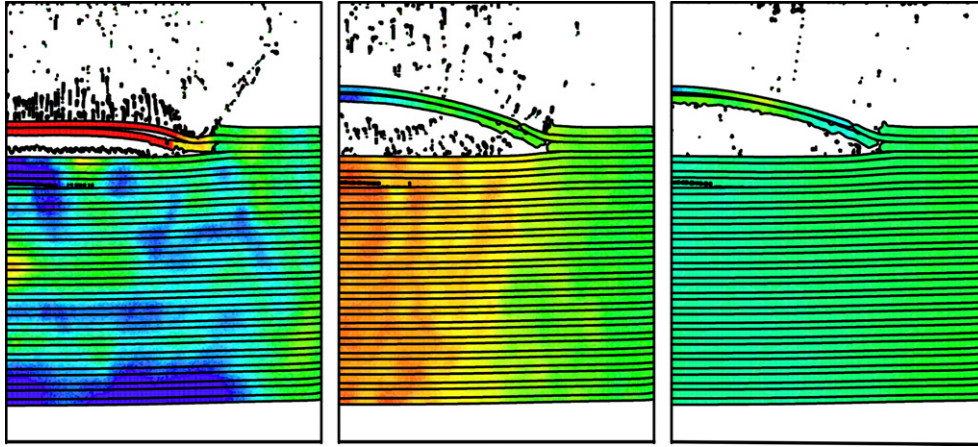


Fig. 12. Vertical velocity at 1, 5 and 25 μs for a composite with uniform layers. Blue indicates a velocity of -10 ms^{-1} and red, $+10 \text{ ms}^{-1}$. (For interpretation of the references to colour in this figure legend, the reader is referred to the web version of this article.)

taken to model the thickness variations in the lamina more accurately. For example, a stochastic model could be created by characterizing the imperfections of a representative set of composite specimens. This is generally not a simple task, even for a simple geometry, and it is labor intensive. The easier procedure of directly importing the microstructure from a micrograph [23] circumvents most of the issues associated with constructing a synthetic geometry and avoids most of the labor.

The multi-material arbitrary Lagrangian Eulerian (MM-ALE) formulation [14,15] makes importing digitized images especially easy. Unlike a traditional Lagrangian finite-element formulation [14], which requires the mesh lines to follow the material boundaries, the MM-ALE mesh is chosen to be a uniform, logically regular grid of quadrilateral elements and the material boundaries run through the elements. Associated with each element is a list of the materials it contains, their volumes and their other state variables (density, internal energy, stress, etc.). The material boundaries are generated from the list of materials and their volumes using a volume of fluid (VOF) interface reconstruction algorithm [24]. The problem of importing the geometry from a digital image is therefore reduced to finding the volume of each material that lies within each element.

Digitized images are defined in terms of their pixels, squares of uniform size that are encoded with the grayscale or color components of the image. For the purposes of this research, the images are converted to 8-bit grayscale that gives a range of 256 shades of gray. Each material is associated with an interval in the grayscale, e.g. the Al might be assigned the interval [0,151], and the Ni, the remainder. The appropriate intervals must be determined by inspection since the range of a particular material depends on how the sample was prepared and imaged.

The volume of a particular material in an element is determined by summing up the volume of the intersection of the element with the individual pixels that are within

the material's grayscale range. As shown in Fig. 13, elements are not necessarily an integer number of pixels in size. The thick and thin lines represent the elements and pixels, respectively, and the gray pixels *A*, *B*, and *C* show three cases of pixels being split by elements. Since both the pixel and the element are rectangles with their edges aligned with the global coordinate axes, calculating the volume intersection V is not difficult:

$$V = (x_{\text{right}} - x_{\text{left}}) \cdot (y_{\text{top}} - y_{\text{bottom}}) \quad (21)$$

$$x_{\text{right}} = \min(x_{\text{right}}^{\ell}, x_{\text{right}}^p) \quad (22)$$

$$x_{\text{left}} = \max(x_{\text{left}}^{\ell}, x_{\text{left}}^p) \quad (23)$$

$$y_{\text{top}} = \min(y_{\text{top}}^{\ell}, y_{\text{top}}^p) \quad (24)$$

$$y_{\text{bottom}} = \max(y_{\text{bottom}}^{\ell}, y_{\text{bottom}}^p) \quad (25)$$

where the superscripts p and ℓ refer to pixel and element, respectively, and the subscripts refer to the appropriate edge. During the analysis, the interface reconstruction algorithm generates material interfaces according to the material volumes present in the elements [14,25].

Fig. 15 shows the initial conditions for the simulation employing the imported lamina geometry from the first millimeter from the left of Fig. 14a, and Fig. 16 shows

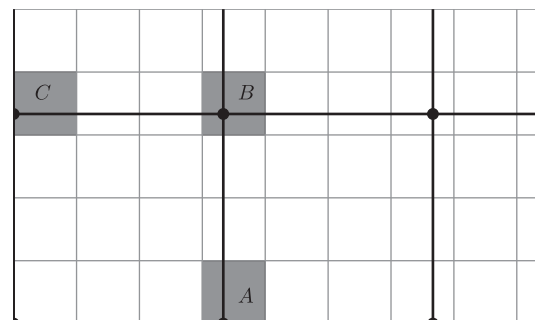
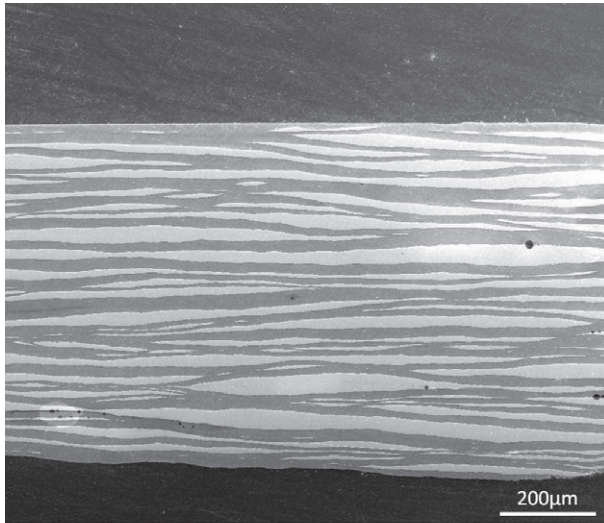
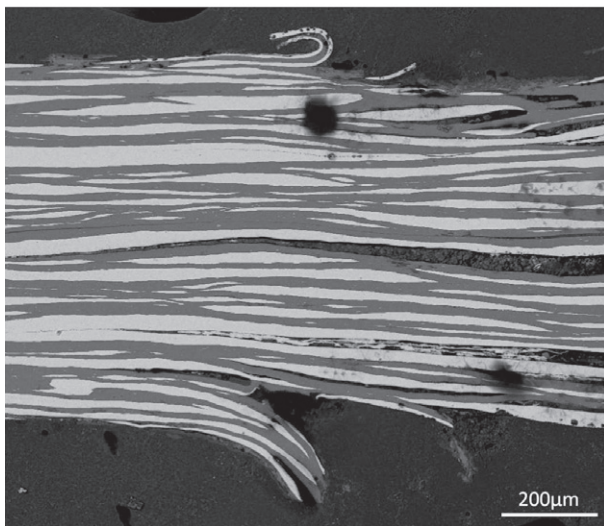


Fig. 13. Pixels split by elements.



(a) Initial State



(b) Post-shock State

Fig. 14. Initial and final states. It should be mentioned that sectioning the sample destroys it, thus the final state is not from the same sample as the initial state.

the sequence for the fully bonded simulation at 1, 5 and 25 μs .

The spallation of the top layers is apparent; however, the distribution of the velocity at time 5 μs is not as uniform as the one indicated in Fig. 12. On the other hand, the entire left side of the composite has a relative velocity with respect to the right side in the final state that is less pronounced in the previous simulation. The shape of the shock wave is better preserved in the idealized geometry, while it experiences a higher degree of diffusion in the less regular geometry found in the real material.

As in the previous case, only the behavior of the top layers seems to agree with the experimental results. From a geometric point of view, Fig. 16 does not seem to provide an apparent improvement with respect to the results obtained in Fig. 12; however, the different velocity distribu-

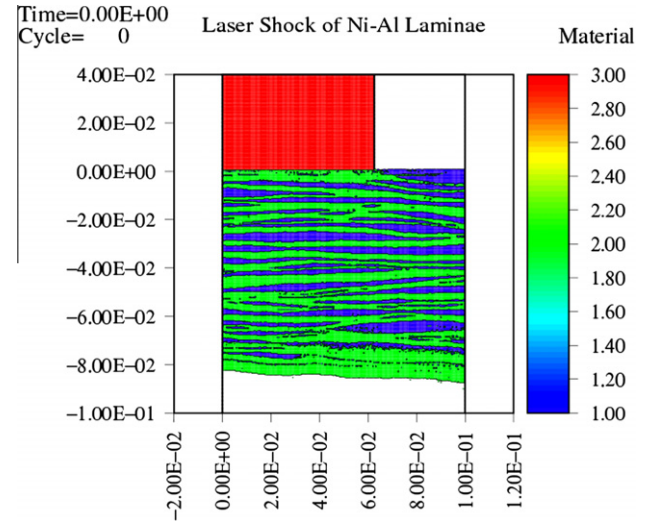


Fig. 15. Initial configuration imported from Fig. 14a.

tion suggests that the laminae geometry plays an important role in the mechanical response of the laminate.

5. Sensitivity to interface bonding

The effects of interface bonding were explored by considering the limiting cases of perfect bonding, no bonding and bonding with a specific failure strength. Section 4 demonstrated that the geometry of the Al and Ni laminae plays an important role in defining the velocity distribution inside specimen. Therefore, since the imported micrography fits the real geometry of the specimen better than the idealized geometry, the former is used in this section.

5.1. Fully bonded

The simulation presented in Section 4 assumes the composite laminae are perfectly bonded (see Fig. 16). The spallation at the top of the specimen agreed with the post-mortem state of the specimen displayed in Fig. 14b. However, the more significant spallation situated at the bottom of the specimen, as well as the delamination of the specimen, are not observed in the simulation.

5.2. Unbonded

Fig. 17 shows the simulation results assuming unbonded laminae. Fractured segments of laminae with high residual velocity occur on the left side of the specimen at time 25 μs . This is a consequence of the lack of interlaminar bonding, which allows the laminae to bend independently and generate high stresses. The localized stress fractures the laminae into segments, which exit the domain of the simulation, removing momentum from the specimen with the consequent loss of velocity.

Fig. 17 displays all the characteristics present in the post-mortem state of the specimen in Fig. 14b: top and

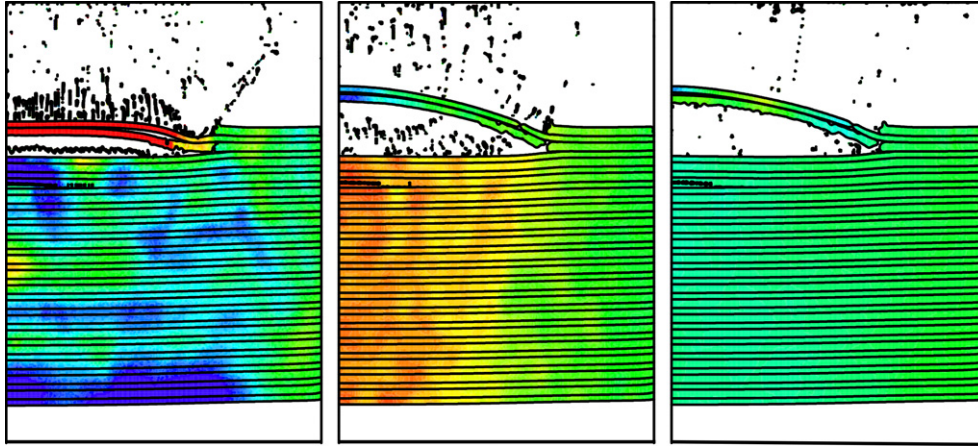


Fig. 16. Vertical velocity for perfectly bonded laminae at 1, 5 and 25 μs . Blue indicates a velocity of -10 ms^{-1} and red, $+10 \text{ ms}^{-1}$. (For interpretation of the references to colour in this figure legend, the reader is referred to the web version of this article.)

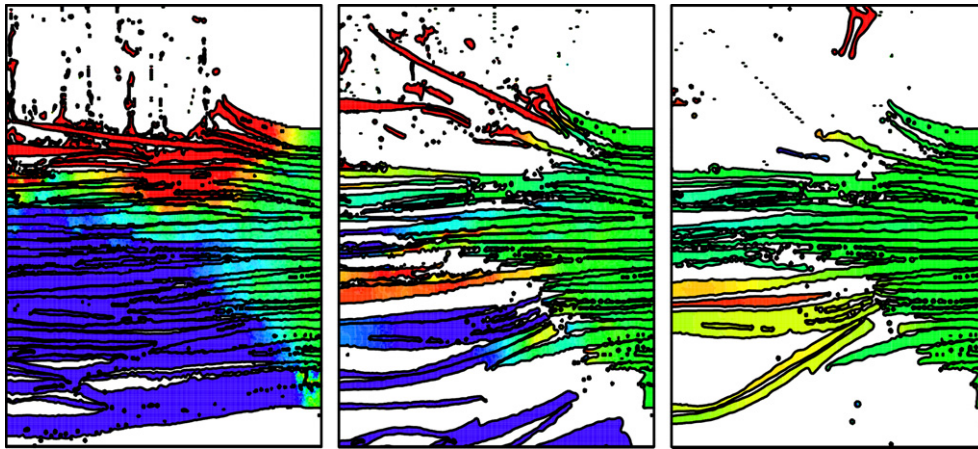


Fig. 17. Vertical velocity for unbonded laminae at 1, 5 and 25 μs . Blue indicates a velocity of -10 ms^{-1} and red, $+10 \text{ ms}^{-1}$. (For interpretation of the references to colour in this figure legend, the reader is referred to the web version of this article.)

bottom spallation, and delamination. However, the level of damage and the amount of spalled material is greater than in Fig. 14b, and the delamination is not entirely representative.

5.3. Bonding with a prescribed failure strength

In this model, the bonding between a pair of materials fails when the stress normal to the materials interface exceeds the prescribed bonding strength. The bonding between materials in the finite-element simulation is enforced by coupling their nodal velocities and accelerations [17–19], and therefore the bond failure is imposed at the nodal level. The stress at a node between two materials is calculated from the volume-weighted average of the stresses and the normal direction:

$$t_{A_{int}}^{(i,j)} = \mathbf{n}_A^{(i,j)} \cdot \sum_{\substack{E \in E_A \\ E \in E_{int}^{(i,j)}}} \frac{(\sigma_E^i V_E^i + \sigma_E^j V_E^j)}{(V_E^i + V_E^j)} \mathbf{n}_A^{(i,j)} \quad (26)$$

where $t_{A_{int}}^{(i,j)}$ is the stress normal to the interface between material i and material j at node A , $\mathbf{n}_A^{(i,j)}$ is the unit vector normal to the interface, σ_E^i is the stress in element E for material i , V_E^i is the volume, E_A is the set of elements sharing node A , and $E_{int}^{(i,j)}$ is the set of elements containing the interface between material i and material j . Failure occurs when:

$$t_{A_{int}}^{(i,j)} \geq t_b, \quad (27)$$

where t_b is the interface bond strength. The velocities and accelerations of the two materials are not coupled at node A when the condition of Eq. (27) is satisfied, and, as a result, the two materials are free to move apart from each other.

Fig. 18 shows the results of the simulation that employed a prescribed bonding strength of 120 MPa between the Al and Ni laminae.

The amount of spalled material from the top and bottom of the specimen in Fig. 18 at time 25 μs agrees with the experimental results shown in Fig. 14b. However, the

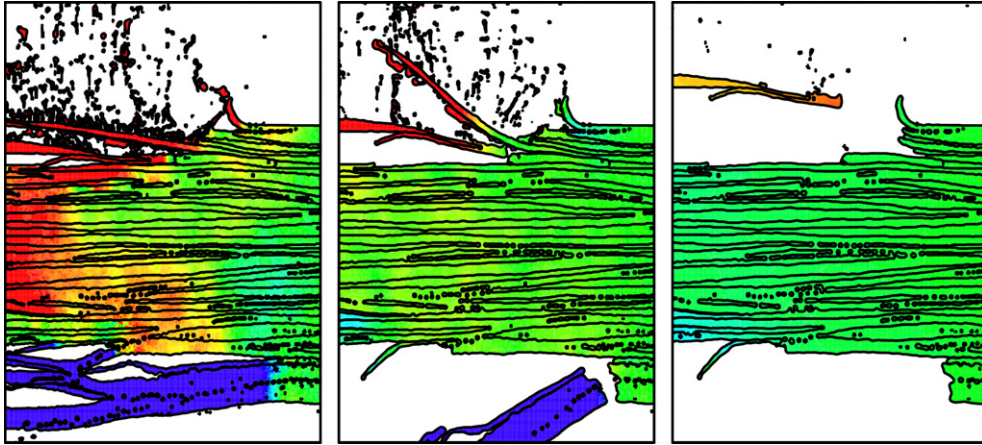


Fig. 18. Vertical velocity for the interface bonding with failure model at 1, 5 and 25 μs . Blue indicates a velocity of -10 ms^{-1} and red, $+10 \text{ ms}^{-1}$. (For interpretation of the references to colour in this figure legend, the reader is referred to the web version of this article.)

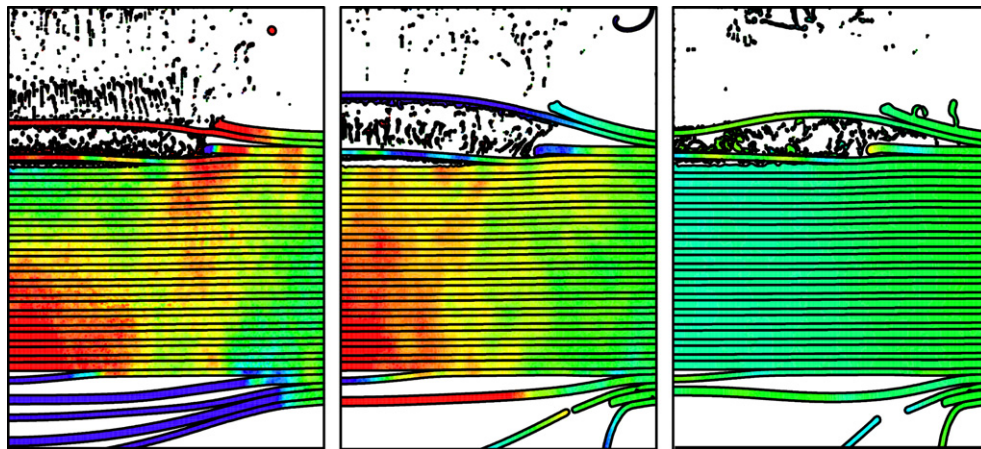


Fig. 19. Vertical velocity of uniform laminae with interface bond failure at 1, 5 and 25 μs . Blue indicates a velocity of -10 ms^{-1} and red, $+10 \text{ ms}^{-1}$. (For interpretation of the references to colour in this figure legend, the reader is referred to the web version of this article.)

number of curved ends in the fractured laminae is lower in Fig. 18 than in Fig. 14b, and the simulation does not show signs of delamination. As expected, the level of damage in Fig. 18 falls in between the levels of damage in Figs. 16 and 17. In particular, Fig. 18 does not display the large amount of damage observed in Fig. 17, and the residual velocity in the specimen is lower than in Fig. 16 (i.e. the laminae fragments removed momentum as they separated from the specimen). Overall, this simulation provided results that are in good agreement with the experiment.

For completeness, Fig. 19 shows the results of combining the ideal laminae geometry with the 120 MPa bond strength. The amount of spalled material at the top and bottom of the specimen is less than in Fig. 18. Numerous Al fragments are present between the top two Ni laminae at time 25 μs due to the fully damaged Al lamina that was observed in Fig. 11. A certain degree of delamination is observed, but it is confined near the top and bottom, while the post-mortem micrograph on the experimental specimen of Fig. 14b shows some delamination in the mid-

dle of the specimen. The results observed in Fig. 19 are improved with respect to Fig. 12; however, the imported micrograph of Fig. 18 provides a more realistic result.

6. Conclusions

The objective of this investigation was to establish the dynamic mechanical properties and damage mechanisms in Ni–Al laminates produced by successive roll bonding. A novel experimental approach, laser shock compression with associated spalling and fragmentation, was used. It is shown that the tensile strength of the Ni–Al interfaces is much lower than that of the highly cold-rolled laminates. The combined experimental and numerical experiments established the effects that the geometry of the laminate constituents and the interlaminar bonding between Al and Ni have on the numerical solution; both aspects played an important role in predicting the mechanical response of specimen. The geometry of the Al and Ni laminae proved to be an important factor in describing the velocity distri-

bution in the specimen, and the interlaminar bonding affected the amount of material spalled from the specimen.

These results are also useful to those interested in improving the mechanical properties of this class of materials since our calculations show that a laminate having “perfect” geometry (uniform laminae) with “perfect bonding” is substantially stronger than the experimental material.

Acknowledgments

This research was supported by ONR MURI Grant N00014-07-1-0740. We thank Prof. T. Weihs for providing us the specimens. We thank the Jupiter Laser Facility at LLNL for the use of the Janus platform for carrying out the laser shock experiments. They were carried out by Drs. B.R. Maddox and M.A. Meyers. Dr. D. Correll, Director of ILSA, was instrumental in enabling its use. Discussions with Prof. V.F. Nesterenko are gratefully acknowledged.

References

- [1] Wei CT, Maddox BR, Weihs TP, Stover AK, Nesterenko VF, Meyers MA. In: 16th APS topical conference on shock compression of condensed matter; 2009. p. 305–8.
- [2] Wei CT, Maddox BR, Stover AK, Weihs TP, Nesterenko VF, Meyers MA. *Acta Mater* 2011;59:5276–87.
- [3] Stover AK, Walker NK, Knepper R, Fritz GM, Hufnagel TC, Weihs TP. In: JANNAF conference, Boston; 2008.
- [4] Jarmakani H, Maddox B, Wei CT, Kalantar D, Meyers MA. *Acta Mater* 2010;58(14):4604–28.
- [5] Zhu WH, Yoshida M, Tamura H, Kondo K, Tanimura S. *J Mater Sci Lett* 2001;20:961–3.
- [6] Grady DE. *J Mech Phys Solids* 1988;36(3):353–84.
- [7] Kipp ME, Grady DE, Swegle JW. *Int J Impact Eng* 1993;14:427–38.
- [8] Meyers MA, Chawla KK. *Mech Behav Mater* 1994.
- [9] Sherman D, Gong X. *J Mater Res* 2001;16(3):721–7.
- [10] Grady DE. *J Appl Phys* 1990;53:322–5.
- [11] HYADES computer program, PP.06.06. Cascade Applied Sciences Inc., address Golden, CO, USA; 2006.
- [12] Glenn LA, Chudnovski AJ. *J Appl Phys* 1986;59:1379–80.
- [13] Zhou F, Molinari JF, Ramesh KT. *Comput Mater Sci* 2006;37:74–85.
- [14] Benson DJ. *Comput Methods Appl Mech Eng* 1992;99:235–394.
- [15] Benson DJ. *Comput Mech* 1995;15:558–71.
- [16] Benson DJ. *Comput Methods Appl Mech Eng* 1997;140:59–86.
- [17] Vitali E, Benson DJ. *Int J Numer Methods Eng* 2006;67(10):1420–44.
- [18] Vitali E, Benson DJ. *Int J Numer Methods Eng* 2008;76(6):893–921.
- [19] Vitali E, Benson DJ. *Comput Mech* 2009;43(6):847–57.
- [20] Vitali E, Benson DJ. *Comput Mech*, submitted for publication.
- [21] Johnson GR, Cook WH. *Eng Fract Mech* 1985;21(1):31–48.
- [22] Steinberg D. Report UCRL-MA-106439, Lawrence Livermore National Laboratory; 1996.
- [23] Benson DJ, Conley P. *Model Simul Mater Sci Eng* 1999;7:333–54.
- [24] Benson DJ. *Appl Mech Rev* 2002;55(2):151–65.
- [25] Youngs D. *Numer Methods Fluid Dynam* 1982:273–85.